nature research

https://doi.org/10.1038/s41567-020-1031-5

Supplementary information

Entanglement between distant macroscopic mechanical and spin systems

In the format provided by the authors and unedited

Supporting Information

Entanglement between Distant Macroscopic Mechanical and Spin Systems

Rodrigo A. Thomas,* Michał Parniak,* Christoffer Østfeldt,* Christoffer B. Møller,*,† Christian Bærentsen, Yeghishe Tsaturyan,‡ Albert Schliesser, Jürgen Appel,§ Emil Zeuthen, and Eugene S. Polzik¶
Niels Bohr Institute, University of Copenhagen, Copenhagen, Denmark

CONTENTS

A. Experimental setup SI 1
1. Atomic spins SI 1
2. Optomechanics SI 2
3. Hybrid system matching & homodyne detection SI 4

B. Theoretical model SI 5
1. Atomic ensemble SI 6
2. Optomechanics SI 7
3. Hybrid system I/O relations SI 9

C. Wiener filtering SI 10

D. Entanglement estimation SI 12

E. Uncertainties SI 13

References SI 16

Appendix A: Experimental setup

1. Atomic spins

The atomic spin oscillator is prepared in a 50 °C warm ensemble of caesium atoms, confined in a spin anti-relaxation-coated microcell [1] (300 µm × 300 µm cross-section and 10 mm in length). The natural linewidth, in the absence of light, is $\gamma_{\mathrm{S0,dark}} = 1/(\pi T_2) = 450\,\mathrm{Hz}$, as measured by pulsed Magneto-Optical Resonance Signal (MORS) [2].

The microcell is positioned in a magnetic shield equipped with coils producing a homogeneous magnetic bias field orthogonal to the probe direction, and a heater to keep the interior at the desired temperature, effectively determining the total atom number. The magnetic field direction sets the quantization axis, denoted as the x-direction. The high thermal mass of the shield ensures a stable temperature throughout the experimental trials. The resonance frequency of the spin $|\omega_{\mathrm{S}}|$, i.e., the Larmor frequency, is controlled by the magnitude of the magnetic field.

The atoms travel through a Gaussian mode of the probe laser focused at the center of the microcell, with the beam waist ($w_0 \approx 80\,\mu\mathrm{m}$) optimised to maximise the filling factor without incurring extra optical losses. The laser frequency is blue-detuned by 3 GHz from the $F = 4 \rightarrow F' = 5$ D_2 transition. Even at this detuning the tensor interaction is non-negligible, which requires a careful choice of the input linear polarisation. The chosen polarisation is at the angle $\alpha \approx (60 \pm 2)^\circ$ with respect to the magnetic field such that the tensorial Stark shifts induced by the probe cancel the quadratic Zeeman splitting $\omega_{\mathrm{qzs}}/2\pi = 400\,\mathrm{Hz}$, as described by the atomic polarisability tensor (see Supplementary Information (SI) B 1 for more details).

The standard quantum Stokes variables $\hat{S}_x, \hat{S}_y, \hat{S}_z, \hat{S}_0$ – representing the light electric field in terms of its linear, diagonal, and circular polarisation states [3] and the total intensity – are redefined as $\{\hat{S}_\parallel = \hat{S}_x \cos 2\alpha - \hat{S}_y \sin 2\alpha, \hat{S}_\perp = \hat{S}_x \sin 2\alpha + \hat{S}_y \cos 2\alpha, \hat{S}_z, \hat{S}_0\}$. When mapping the polarisation variables into quadrature variables, we choose the parallel component as the classical variable – the local oscillator LO_1 with the photon flux $\langle \hat{S}_\parallel \rangle = \langle \hat{S}_0 \rangle = S_\parallel$, leaving

$\hat{S}_\perp, \hat{S}_z$ as quantum variables. We define the light quadratures as $\hat{X}_\mathrm{L} = \hat{S}_z/\sqrt{S_\parallel}$ and $\hat{P}_\mathrm{L} = -\hat{S}_\perp/\sqrt{S_\parallel}$. The photon flux determines the readout rate $\Gamma_\mathrm{S}/2\pi \propto J_x S_\parallel$ and the power broadening decoherence rate $\gamma_\mathrm{pb}/2\pi \propto S_\parallel$. In the experiment, the LO_1 power is $\sim 350\,\mu\mathrm{W}$. The decoherence rate of the oscillator is also affected by the optical pumping process, represented by the contribution γ_op. The total bandwidth of the spin resonance in the absence of dynamical processes is $\gamma_\mathrm{S0} = \gamma_\mathrm{S0,dark} + \gamma_\mathrm{pb} + \gamma_\mathrm{op}$. For the conditions of the current experiment, the ratio of quantum backaction to thermal noise contributions is $\mathrm{QBA/TH} = 4.9$.

As the atoms move in and out of the beam, the scattered photons couple to various atomic motional modes. The motion of the atoms is fast (flight-through time $\sim$1 µs) and uncorrelated, leading to a motionally averaged coupling [4]. Phenomenologically, the long-lived correlations give rise to the mean spin mode – the mode of interest – and the short-time correlations to an uncorrelated spin contribution – the broadband spin mode. In the regime of operation both optical responses are harmonic, with the susceptibility of short-time correlations following a low-Q damped harmonic oscillator type, with resonance frequency Ω_S and linewidth $\gamma_\mathrm{bb}/2\pi \sim 1\,\mathrm{MHz}$ and coupling rate $\Gamma_\mathrm{S,bb}$.

We observe the response of the two spin modes to coherent drive tones $\hat{X}^\mathrm{drive}_\mathrm{L,S}$ in Figures SI1(a) and SI1(b) for different input modulation types $\hat{X}^\mathrm{drive}_\mathrm{L,S} = \hat{X}^\mathrm{in}_\mathrm{L,S}\cos\vartheta_\mathrm{in} + \hat{P}^\mathrm{in}_\mathrm{L,S}\sin\vartheta_\mathrm{in}$, measured by Coherent Induced FAraday Rotation (CIFAR) [5], a calibration technique which is inspired by the OptoMechanically Induced Transparency (OMIT) [6]. In short, CIFAR references the phase-sensitive response of the spin to an oscillating input polarisation at ω_RF; to the first order, the resulting interference between the drive and response, for $\Gamma_\mathrm{S}/\gamma_S \gg 1$ and $\vartheta_\mathrm{in} = \pm\pi/4$, gives rise to a dispersive feature in the detected field, with maximum destructive interference at $\pm\Gamma_\mathrm{S}$ away from $|\omega_\mathrm{S}|$. Under the assumption that both modes are uncorrelated, we fit these data to the input-output relations (equation (SI B.14)), allowing us to extract the readout rate Γ_S. The backaction on the broadband mode is negligible, i.e., $\Gamma_\mathrm{S,bb}/\gamma_\mathrm{S,bb} \ll 1$. For all noise spectra, we treat the broadband contribution as constant in the frequency range of interest, added incoherently with all other noise processes; effectively, it acts as added phase noise in the phase quadrature of light. The added spectral power at the resonance frequency due to extra spin noise, corrected for losses, is $\overline{S}_\mathrm{S,bb} = 1.68$ SN units. This noise depends on spatial properties of the beam and could be reduced by using a cell with larger cross section perfectly filled with a flat-top probe laser beam.

The spin oscillator is prepared by optically pumping the ensemble towards the $|F = 4, m_F = 4\rangle$ Zeeman sublevel. A repump laser is tuned to the $F = 3 \to F' = 2$ hyperfine transition in the D_2 line and a pump laser to the $F = 4 \to F' = 4$ hyperfine transition in the D_1 line, both circularly polarised. The pump laser directly couples to the coherences of interest, competing with the decoherence and depumping caused by the probe, adding $\gamma_\mathrm{op}/2\pi \sim 1\,\mathrm{kHz}$. The spin polarisation $p = 0.82 \pm 0.01$ is characterised by pulsed MORS [2], with the spectrum shown in Figure SI1(c). Due to the dominant role of the probing and pumping lasers, the Zeeman population distribution does not follow the spin temperature model. The fitting model follows Eq. (17) from Ref. [2] for arbitrary Zeeman population distribution. The spin polarisation is determined by assuming that the population of $|F = 4, m_F = -4\rangle$ is negligible, which is guaranteed by the presence of the resonant pump laser. The spin oscillator variables $\hat{X}_\mathrm{S} = \hat{J}_z/\sqrt{\hbar J_x}$ and $\hat{P}_\mathrm{S} = -\hat{J}_y/\sqrt{\hbar J_x}$ are defined according to the steady-state spin polarisation, which defines J_x. From the population distribution we calculate the variance of the spin components, which leads to the added spin thermal occupancy $n_\mathrm{S} = 0.8$, meaning that incoherent processes drive towards an equilibrium with $\mathrm{Var}[\hat{X}_\mathrm{S}] = \mathrm{Var}[\hat{P}_\mathrm{S}] = n_\mathrm{S} + 1/2$.

The spin system can be operated in two regimes, which differ only by their effective masses. Optical pumping of the atoms to the highest energy state, i.e. spins aligned parallel with the bias magnetic field, leads to an effective negative mass, whereas pumping to the lowest energy state, i.e. spin aligned anti-parallel to the bias field, leads to an effective positive mass [7]. This choice defines the sign of the atomic susceptibility χ_S.

2. Optomechanics

The optomechanical system consists of a 13 nm thick, highly stressed, phononically patterned silicon nitride membrane featuring a soft-clamped [8], localised out-of-plane vibrational mechanical mode with a cryogenic Q-factor of 0.65×10^9 and resonance frequency of 1.37 MHz. This membrane is positioned close to the waist of a 2.6 mm long optical cavity along its axis and with maximum spatial overlap between the cavity mode and the localised mechanical mode. The cavity consists of two mirrors with 25 mm radius of curvature, and power transmissions of 20 ppm and 360 ppm, respectively. The entire optomechanical assembly is placed in a liquid helium flow cryostat, which is cooled to 4.4 K.

The basis of the light-mechanics coupling is the radiation pressure force of light on the membrane whose out-of-plane motion causes a dispersive shift of the cavity resonance frequency [9]. The placement of the membrane inside the cavity divides it into two sub-cavities, where the amount of light in each depends on the membrane position.

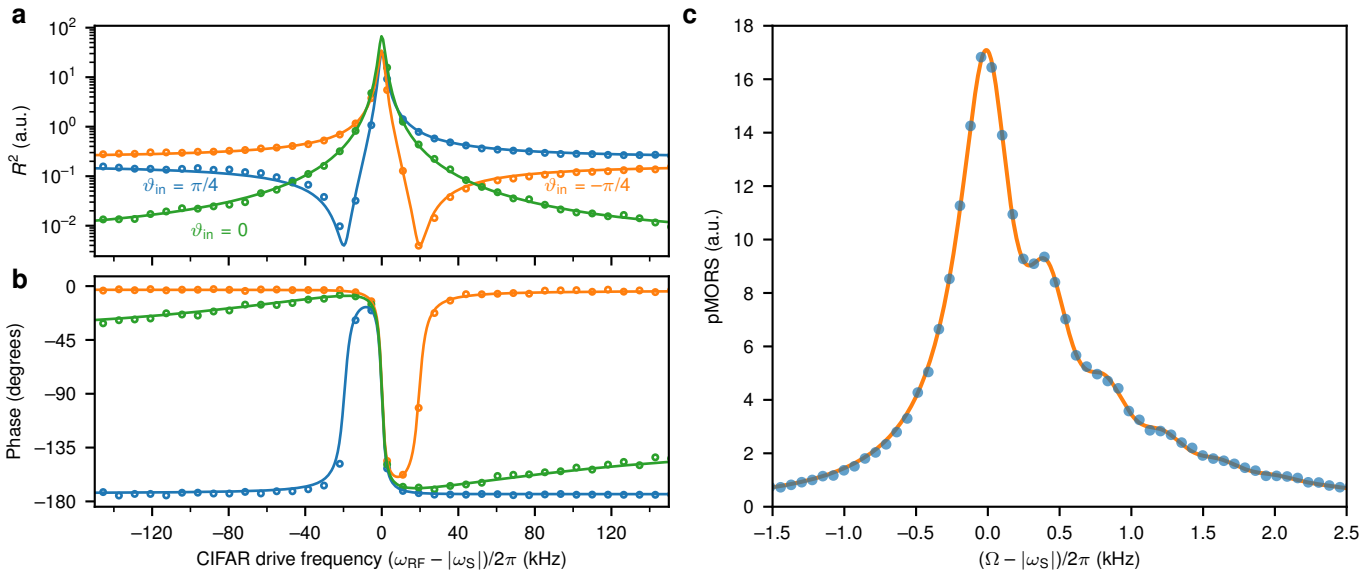

Figure SI1. **Spin oscillator calibrations.** **a** and **b** show the square amplitude (R^2) and phase of the demodulated spin response to a coherently driven light field with different θ_{in}. **c,** pulsed MORS spectrum for the distribution of atoms in the Zeeman levels corresponding to $p = 0.82 \pm 0.01$.

This system can be formally treated as a canonical end-mirror optomechanical system with just a single intracavity optical field. In this formalism adjusting the lengths of each subcavity, periodically modulates the canonical cavity parameters of optical linewidth, κ, resonance frequency, overcoupling κ_{in}/κ (where κ_{in} is the coupling rate of the input mirror), as well as the optomechanical single-photon coupling rate g_0.

The sub-cavities can be independently and electronically fine-tuned so as to simultaneously realise a high cooperativity optomechanical system, as well as tunability, in order to set an appropriate cavity detuning with respect to the probe of the atomic spin system. The various canonical optomechanical parameters are characterised through several independent measurements and a full list of these system parameters can be seen in Table SI1.

The cavity linewidth is characterised first by measuring the optical amplitude quadrature beatnote of a phase-modulation sideband transmitted through the cavity. In a second method, a single carrier is scanned across the cavity resonance on a timescale comparable to the cavity response time and the resultant beating ringdown signal is observed.

The cavity detuning is determined by combining the characterisation of the cavity dither lock error signal and knowledge of the cavity linewidth. By locating the turning point of the dither error signal we translate our locked error signal amplitude into an absolute detuning.

The effective mechanical bath temperature and field-enhanced optomechanical coupling rate $g = g_0|\alpha|$, where α is intra-cavity field, can be obtained by fitting the full optomechanical model to the ponderomotive squeezing spectra, seen in Fig. SI2. These spectra result from pumping the cavity from the high-reflector port and detecting the optical amplitude quadrature in transmission through the highly overcoupled port [10]. We fit the model to these two spectra simultaneously, using separately measured values for Δ, κ, and Q. From this characterisation the detection efficiency, with and without LO_3, can similarly be inferred. We observed up to 3 dB of ponderomotive squeezing. We note that while our system is not optimised for measuring maximum ponderomotive squeezing, nor operated in the optimum regime, we observe close to record amounts of squeezing for optomechanical systems.

A new feature of our optomechanical cavity compared to our previous work [7] is the full electronic control over the position of the membrane inside the standing wave of the cavity. Two piezos, each with an effective travel length of well over a half-wavelength at cryogenic conditions, allow us to scan the lengths of the two sub-cavities, so as to effectively position the membrane at any given intra-cavity position while keeping the cavity on resonance with the optical light field. By monitoring the cavity transmission as we scan the position of the membrane, we obtain knowledge about the position within the standing wave. We operate the optomechanical system at the point of highest total cavity linewidth, giving us the best overcoupling in reflection, as well as a high coupling rate g_0.

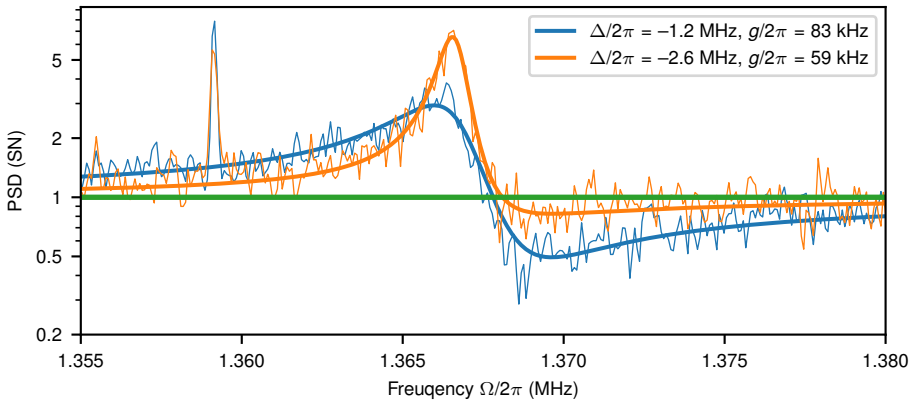

Figure SI2. **Ponderomotive squeezing spectra for different cavity detunings.** From these spectra we infer g, T, optical losses in the detection path etc. See SI A 2 for details. Using other system parameters, measured independently, we obtain an effective bath temperature of $T = (11.4 \pm 0.5)\,\mathrm{K}$.

3. Hybrid system matching & homodyne detection

The overall hybrid system consists of the cascaded optical readout of the spin and mechanical system by an itinerant light field, as outlined in the main text, see Fig. 2.

After interacting with the spin, LO_1 is filtered off the quantum signal, which is orthogonally polarisation to LO_1. The quantum signal is spatially overlapped with LO_2 on a PBS, after which the two beams co-propagate, but have different polarisation. To remedy this, we use a $\lambda/2$ plate and a second PBS to reject most of the LO_2 beam and retain most of the quantum signal, incurring a small (percent-scale) loss of the quantum signal. This directly translates the polarisation quadrature operators that interacted with the spin system into the amplitude and phase quadratures that are now coupled to the membrane-in-the-middle optomechanical system, in which radiation pressure of the LO_2 drives the mechanical oscillator.

The cascaded system, including the double pass nature of our atomic read out, makes our system susceptible to back-reflections from the optomechanical system to the spin system, since these reflections effectively amount to a self-driving force on the spins, leading to self-induced oscillations of the spin system. Therefore, the system necessitates the introduction of an optical isolator, leading to additional optical intersystem losses. Further, non-perfect rejection of LO_1 by the PBS separating LO_1 and the quantum signal leads to a part of LO_1 co-propagating with LO_2. These two LOs interfere, which effectively turns drifts in the LO_1-LO_2 phase φ into changes of the total optical power sent to the mechanical system.

The optical output of the spin system is spatially mode matched to the optomechanical cavity by using LO_1 as a proxy. By rotating waveplates, the LO_1 probe is directed to the cavity and modematched to it. The degree of modematching is characterised by the amount of ponderomotive squeezing observed in the optical amplitude quadrature in reflection.

Phase fluctuations of the light reflected off the optomechanical cavity are measured with homodyne detection as depicted in Fig. 2 of the main text. The reflected beam is spatially overlapped with LO_3 on a polarising beamsplitter (PBS), and the LO_3 is mode matched to the optical signal. The LO_3 and LO_2 plus quantum fluctuations are now co-propagating, but in different polarisation channels. They are transmitted through a $\lambda/2$ waveplate, set to rotate the polarisations by 45°. The mixed polarisation components are then respectively transmitted and reflected off the second PBS. Neglecting interference, this splits both components equally into the two ports. The total set of PBS-$\lambda/2$-PBS thus acts as an effective 50:50 beamsplitter. The light fields are now in the correct polarisation channels to interfere for homodyne detection.

We perform differential detection, by measuring the photocurrents of a photodetector in each arm, and electronically subtracting the two currents. The slow component is fed back to a piezo, controlling the optical path in the LO_3 arm, thus determining the homodyne detection angle ϑ. The optical powers are $\sim 2\,\mathrm{mW}$ of LO_3 and $\sim 9\,\mu\mathrm{W}$ of LO_2.

Experimental spectra are presented in the main text, Figs. 3 and 4, as well as in Figs. SI4 and SI8. In Fig. SI4 we present a wider frequency range, thus showing features such as out-of-bandgap mechanical modes, mechanical modes of the mirror substrates, higher-order mechanical modes in the bandgap, etc. In Fig. SI8 we present experimental

spectra plus model fits for all atomic detunings presented in Fig. 4.

Appendix B: Theoretical model

In this section we will present the model used to fit the experimental data and to extract parameters necessary for the entanglement analysis and Wiener filtering. The latter also relies on signal and noise (cross-)correlation functions calculated from the (fitted) model.

For a function in the time domain $\hat{f}(t)$, we use the Fourier transform sign convention and property

$$\hat{f}(\Omega) = \mathcal{F}\{\hat{f}(t)\} = \int_{-\infty}^{\infty} \hat{f}(t) e^{i\Omega t}\, \mathrm{d}t, \qquad \mathcal{F}\left\{\frac{\mathrm{d}}{\mathrm{d}t}\hat{f}(t)\right\} = -i\Omega \hat{f}(\Omega). \tag{SI B.1}$$

For the localised optical cavity mode, we introduce the photon annihilation and creation operators obeying the commutation relation $[\hat{a}, \hat{a}^\dagger] = 1$, and, in turn, the light amplitude and phase quadratures (suppressing the time/Fourier-frequency dependence for brevity)

$$\hat{X}_\mathrm{L} = \frac{\hat{a} + \hat{a}^\dagger}{2} \qquad \hat{P}_\mathrm{L} = \frac{\hat{a} - \hat{a}^\dagger}{2i}, \tag{SI B.2}$$

which obey the same-time commutation relation $[\hat{X}_\mathrm{L}(t), \hat{P}_\mathrm{L}(t)] = i/2$.

All travelling optical fields, including additional (vacuum) noise fields introduced by optical losses, are described by amplitude and phase quadratures

$$\hat{X}_\mathrm{L}^{\mathrm{in(out)}} = \frac{\hat{a}_\mathrm{in(out)} + \hat{a}_\mathrm{in(out)}^\dagger}{2} \qquad \hat{P}_\mathrm{L}^{\mathrm{in(out)}} = \frac{\hat{a}_\mathrm{in(out)} - \hat{a}_\mathrm{in(out)}^\dagger}{2i}, \tag{SI B.3}$$

defined in terms of the quantum amplitudes

$$\hat{a}_\mathrm{in(out)}(t) = \frac{1}{2\pi}\int_{-\infty}^{\infty} \mathrm{d}\Omega\; e^{-i\Omega t} \hat{a}_\mathrm{in(out)}(\Omega) \qquad \hat{a}_\mathrm{in(out)}^\dagger(t) = \frac{1}{2\pi}\int_{-\infty}^{\infty} \mathrm{d}\Omega\; e^{+i\Omega t} \hat{a}_\mathrm{in(out)}^\dagger(\Omega) \tag{SI B.4}$$

where $\hat{a}_\mathrm{in(out)}$ is the field in a rotating frame with respect to the relevant optical carrier frequency ω_laser, so that $\hat{a}_\mathrm{in(out)}(\Omega)$ represents the field at absolute frequency $\Omega + \omega_\mathrm{laser}$. This expression is valid for Fourier frequencies close to the optical carrier, $|\Omega| \ll \omega_\mathrm{laser}$. According to the above considerations the Fourier transforms of the rotating-frame operators $\hat{a}_\mathrm{in(out)}(t)$ and $\hat{a}_\mathrm{in(out)}^\dagger(t)$ (see Eqs. (SI B.4)), using the convention in Eq. (SI B.1), are

$$\mathcal{F}\{\hat{a}_\mathrm{in(out)}(t)\} = \hat{a}_\mathrm{in(out)}(\Omega), \quad \mathcal{F}\{\hat{a}_\mathrm{in(out)}^\dagger(t)\} = \hat{a}_\mathrm{in(out)}^\dagger(-\Omega). \tag{SI B.5}$$

The non-vanishing commutation relations of the travelling field operators are $[\hat{X}_\mathrm{L}^{\mathrm{in(out)}}(t), \hat{P}_\mathrm{L}^{\mathrm{in(out)}}(t')] = (i/2)\delta(t-t')$. Accordingly, the symmetrised power spectral densities of the incoming vacuum light fields are

$$\overline{S}_{X_\mathrm{L}X_\mathrm{L}}(\Omega)\delta(\Omega-\Omega') = \frac{1}{2}\langle \hat{X}_{\mathrm{L},j}^{\mathrm{in}\dagger}(\Omega)\hat{X}_{\mathrm{L},j}^{\mathrm{in}}(\Omega') + \hat{X}_{\mathrm{L},j}^{\mathrm{in}}(\Omega')\hat{X}_{\mathrm{L},j}^{\mathrm{in}\dagger}(\Omega)\rangle = \frac{1}{4}\delta(\Omega-\Omega') \tag{SI B.6a}$$

$$\overline{S}_{P_\mathrm{L}P_\mathrm{L}}(\Omega)\delta(\Omega-\Omega') = \frac{1}{2}\langle \hat{P}_{\mathrm{L},j}^{\mathrm{in}\dagger}(\Omega)\hat{P}_{\mathrm{L},j}^{\mathrm{in}}(\Omega') + \hat{P}_{\mathrm{L},j}^{\mathrm{in}}(\Omega')\hat{P}_{\mathrm{L},j}^{\mathrm{in}\dagger}(\Omega)\rangle = \frac{1}{4}\delta(\Omega-\Omega'). \tag{SI B.6b}$$

For the mechanical (M) and spin (S) oscillators, we follow the commutation relation $[\hat{X}_j, \hat{P}_j] = i$ for $(j = \mathrm{M}, \mathrm{S})$; the effect of the thermal reservoirs $\hat{F}_j$ with mean thermal occupancy n_j is captured by the symmetrised correlation functions

$$\overline{S}_{F_S^X F_S^X}(\Omega)\delta(\Omega-\Omega') \equiv \frac{1}{2}\langle \hat{F}_\mathrm{S}^{\mathrm{X},\dagger}(\Omega)\hat{F}_\mathrm{S}^{\mathrm{X}}(\Omega') + \hat{F}_\mathrm{S}^{\mathrm{X}}(\Omega')\hat{F}_\mathrm{S}^{\mathrm{X},\dagger}(\Omega)\rangle = \gamma_{\mathrm{S}0}(n_\mathrm{S}+1/2)\delta(\Omega-\Omega') \tag{SI B.7a}$$

$$\overline{S}_{F_S^P F_S^P}(\Omega)\delta(\Omega-\Omega') \equiv \frac{1}{2}\langle \hat{F}_\mathrm{S}^{\mathrm{P},\dagger}(\Omega)\hat{F}_\mathrm{S}^{\mathrm{P}}(\Omega') + \hat{F}_\mathrm{S}^{\mathrm{P}}(\Omega')\hat{F}_\mathrm{S}^{\mathrm{P},\dagger}(\Omega)\rangle = \gamma_{\mathrm{S}0}(n_\mathrm{S}+1/2)\delta(\Omega-\Omega') \tag{SI B.7b}$$

$$\overline{S}_{F_M F_M}(\Omega)\delta(\Omega-\Omega') \equiv \frac{1}{2}\langle \hat{F}_\mathrm{M}^{\dagger}(\Omega)\hat{F}_\mathrm{M}(\Omega') + \hat{F}_\mathrm{M}(\Omega')\hat{F}_\mathrm{M}^{\dagger}(\Omega)\rangle = 2\gamma_{\mathrm{M}0}(n_\mathrm{M}+1/2)\delta(\Omega-\Omega'). \tag{SI B.7c}$$

The diagrammatic representation of the fields and operations under considerations is presented in Fig. SI3.

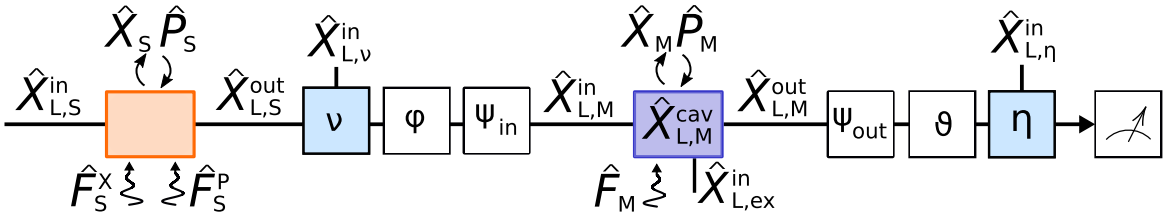

Figure SI3. **Diagramatic representation of the hybrid system.** Various optical fields, operators, thermal bath forces and rotations acting in the hybrid system, from input to detection. Spin (orange box) and mechanical system (blue box) along with driving optical and thermal forces. Light blue boxes represent beam-splitter-like losses. White boxes represent the various rotations applied to the optical fields.

1. Atomic ensemble

The atomic ensemble interacts dispersively with the light, leading to a mutual rotation of the light and spin variables according to the atomic polarizability tensor [11]

$$\hat{H}_{\rm S}/\hbar = -\omega_{\rm S}\hat{J}_x + g_{\rm S}\left[a_0\hat{S}_0\hat{J}_0 + a_1\hat{S}_z\hat{J}_z + 2a_2\left[\hat{S}_0\hat{J}_z^2 - \hat{S}_x(\hat{J}_x^2-\hat{J}_y^2) - \hat{S}_y(\hat{J}_x\hat{J}_y+\hat{J}_y\hat{J}_x)\right]\right], \tag{SI B.8}$$

with a_0, a_1, and a_2 as the relative weights of the scalar, vector and tensor contributions [11], which can be tuned by the detuning of the laser with respect to the atomic resonance and $g_{\rm S}$ is the coupling rate. We work detuned 3 GHz to the blue from the $F = 4 \to F' = 5$ D_2 transition.

In the limit of high spin polarisation in the $F = 4$ hyperfine manifold and for a strong linearly polarised local oscillator polarised at an angle α to the quantization axis, the Hamiltonian can be simplified to [12]

$$\hat{H}_{\rm S}/\hbar = \frac{\omega_{\rm S}}{2}(\hat{X}_{\rm S}^2+\hat{P}_{\rm S}^2) - 2\sqrt{\Gamma_{\rm S}}\left(\hat{X}_{\rm S}\hat{X}_{\rm L}+\zeta_{\rm S}\hat{P}_{\rm S}\hat{P}_{\rm L}\right), \tag{SI B.9}$$

where $\Gamma_{\rm S} = g_{\rm S}^2 a_1^2 S_\parallel J_x$ is the spin oscillator readout rate and $\zeta_{\rm S} = -14\frac{a_2}{a_1}\cos 2\alpha$ is the tensor correction factor, which for our choice of polarisation angle α has a value of ~ 0.028. We have omitted constant energy terms, as they do not affect the dynamics of the spin variables of interest. The canonical light variables are $\{\hat{X}_{\rm L} = \hat{S}_z/\sqrt{S_\parallel}, \hat{P}_{\rm L} = -\hat{S}_\perp/\sqrt{S_\parallel}\}$. In our experimental regime, as $\zeta > 0$, the spin-light interactions deviates from the QND interaction, introducing extra correlation terms and allowing for dynamical cooling of the spin ensemble, effectively changing the decay rate and bath occupation.

The dynamics follows from the Heisenberg-Langevin equations, which, in the steady state and in the frequency space, are

$$\begin{pmatrix} \gamma_{\rm S0}/2+\zeta_{\rm S}\Gamma_{\rm S}-i\Omega & -\omega_{\rm S} \\ \omega_{\rm S} & \gamma_{\rm S0}/2+\zeta_{\rm S}\Gamma_{\rm S}-i\Omega \end{pmatrix}\begin{pmatrix}\hat{X}_{\rm S}\\ \hat{P}_{\rm S}\end{pmatrix} = 2\sqrt{\Gamma_{\rm S}}\begin{pmatrix}0 & -\zeta_{\rm S}\\ 1 & 0\end{pmatrix}\begin{pmatrix}\hat{X}^{\rm in}_{\rm L,S}\\ \hat{P}^{\rm in}_{\rm L,S}\end{pmatrix} + \begin{pmatrix}\hat{F}^{\rm X}_{\rm S}\\ \hat{F}^{\rm P}_{\rm S}\end{pmatrix}, \tag{SI B.10}$$

$$\begin{pmatrix}\hat{X}^{\rm out}_{\rm L,S}\\ \hat{P}^{\rm out}_{\rm L,S}\end{pmatrix} = \begin{pmatrix}\hat{X}^{\rm in}_{\rm L,S}\\ \hat{P}^{\rm in}_{\rm L,S}\end{pmatrix} + \sqrt{\Gamma_{\rm S}}\begin{pmatrix}0 & -\zeta_{\rm S}\\ 1 & 0\end{pmatrix}\begin{pmatrix}\hat{X}_{\rm S}\\ \hat{P}_{\rm S}\end{pmatrix}, \tag{SI B.11}$$

for $2\zeta_{\rm S}\Gamma_{\rm S}$ as the tensor (dynamical) broadening, and $\hat{F}^{\rm X}_{\rm S}, \hat{F}^{\rm P}_{\rm S}$ as the effective force acting on the spins via the thermal bath. We proceed defining the shorthand matrix notation

$$\mathbf{Z} = \begin{pmatrix}0 & -\zeta_{\rm S}\\ 1 & 0\end{pmatrix}, \quad \mathbf{L} = \begin{pmatrix} \gamma_{\rm S0}/2+\zeta_{\rm S}\Gamma_{\rm S}-i\Omega & -\omega_{\rm S} \\ \omega_{\rm S} & \gamma_{\rm S0}/2+\zeta_{\rm S}\Gamma_{\rm S}-i\Omega \end{pmatrix}^{-1},$$
$$\hat{\boldsymbol{X}}^{\rm in(out)}_{\rm L,S} = \begin{pmatrix}\hat{X}^{\rm in(out)}_{\rm L,S}\\ \hat{P}^{\rm in(out)}_{\rm L,S}\end{pmatrix}, \quad \hat{\boldsymbol{X}}_{\rm S} = \begin{pmatrix}\hat{X}_{\rm S}\\ \hat{P}_{\rm S}\end{pmatrix}, \quad \hat{\boldsymbol{F}}_{\rm S} = \begin{pmatrix}\hat{F}^{\rm X}_{\rm S}\\ \hat{F}^{\rm P}_{\rm S}\end{pmatrix}, \tag{SI B.12}$$

and solve the equations for the atomic and light variables

$$\hat{\boldsymbol{X}}_{\rm S} = 2\sqrt{\Gamma_{\rm S}}\mathbf{L}\mathbf{Z}\hat{\boldsymbol{X}}^{\rm in}_{\rm L,S} + \mathbf{L}\hat{\boldsymbol{F}}_{\rm S} \tag{SI B.13}$$

$$\hat{\boldsymbol{X}}^{\rm out}_{\rm L,S} = \hat{\boldsymbol{X}}^{\rm in}_{\rm L,S} + \sqrt{\Gamma_{\rm S}}\mathbf{Z}\hat{\boldsymbol{X}}_{\rm S} = (\mathbf{1}_2 + 2\Gamma_{\rm S}\mathbf{Z}\mathbf{L}\mathbf{Z})\hat{\boldsymbol{X}}^{\rm in}_{\rm L,S} + \sqrt{\Gamma_{\rm S}}\mathbf{Z}\mathbf{L}\hat{\boldsymbol{F}}_{\rm S}, \tag{SI B.14}$$

where $\mathbf{1}_2$ is the 2×2 identity matrix.

In the main text we consider simpler, approximate versions of equations (SI B.13) and (SI B.14) valid in the limit $|\omega_S| \gg \gamma_S, |\Omega - |\omega_S||$. In this limit, the effective thermal forces $\hat{F}_S^X$ and $\hat{F}_S^P$ can be combined into the single thermal force term $\hat{F}_S \approx i\hat{F}_S^X + \hat{F}_S^P$. In this limit, the evolution equation for $\hat{X}_S$ in terms of the susceptibility $\chi_S(\Omega)$ arises from Eq. (SI B.13) (setting $\omega_{S0} \equiv \omega_S$),

$$\hat{X}_S = \chi_S \left[\hat{F}_S + 2\sqrt{\Gamma_S} \begin{pmatrix} 1 \\ -i\zeta_S \end{pmatrix}^\intercal \hat{\boldsymbol{X}}_{L,S}^{in} \right] = \chi_S [\hat{F}_S + 2\sqrt{\Gamma_S}(\hat{X}_{L,S}^{in} - i\zeta_S \hat{P}_{L,S}^{in})], \tag{SI B.15}$$

as presented in the main text. Noting that $\hat{P}_S \approx -\text{sign}(\omega_{S0}) i\hat{X}_S$, the simpler input-output relation discussed in the main text,

$$\boldsymbol{X}_{L,S}^{out} = \boldsymbol{X}_{L,S}^{in} + \sqrt{\Gamma_S} \begin{pmatrix} -i\zeta_S \\ 1 \end{pmatrix} \hat{X}_S, \tag{SI B.16}$$

follows from Eq. (SI B.14).

The CIFAR modelling (see SI A 1) is based on equations (SI B.13) and (SI B.14), with the broadband response added as another atomic mode in the following manner

$$\hat{\mathbf{X}}_{L,S}^{out} = \hat{\mathbf{X}}_{L,S}^{in} + \sqrt{\Gamma_S}\mathbf{Z}\hat{\mathbf{X}}_S + \sqrt{\Gamma_{S,bb}}\mathbf{Z}\hat{\mathbf{X}}_{S,bb} \tag{SI B.17}$$

$$\hat{\mathbf{X}}_{S,bb} = 2\sqrt{\Gamma_{bb}}\mathbf{L}_{bb}\mathbf{Z}\hat{\mathbf{X}}_{L,S}^{in}, \tag{SI B.18}$$

for $\mathbf{L}_{bb}$ as $\mathbf{L}$ with $\gamma_{S0} \to \gamma_{bb}$, $\Gamma_S \to \Gamma_{S,bb}$ and $\Gamma_{S,bb}$ as the broadband response readout rate. Incoherent thermal contributions were disregarded as the input field is modulated with large amplitude. The input field $\hat{\mathbf{X}}_{L,S}^{in}$ quadratures is rotated according to $\hat{\mathbf{X}}_{L,S}^{drive} = O_{\vartheta_{in}} \hat{\mathbf{X}}_{L,S}^{in}$, in which $\boldsymbol{O}_\alpha$

$$\boldsymbol{O}_\alpha = \begin{pmatrix} \cos\alpha & -\sin\alpha \\ \sin\alpha & \cos\alpha \end{pmatrix} \tag{SI B.19}$$

is a rotation matrix. The result of the CIFAR modelling for various ϑ_{in} is presented in Fig. SI1. Fig. SI1(a) shows the amplitude squared R^2 of the detected field; Fig. SI1(b) presents the phase of detected field in respect to the drive.

2. Optomechanics

We start with the standard linearised optomechanical interaction between a mechanical degree of freedom with frequency ω_M and the intracavity field

$$\hat{H}_M/\hbar = \frac{\omega_M}{2}\left(\hat{X}_M^2 + \hat{P}_M^2\right) - \Delta\left(\hat{X}_{L,M}^{cav\,2} + \hat{P}_{L,M}^{cav\,2}\right) - 4g\left(\hat{X}_{L,M}^{cav}\cos\psi_{in} + \hat{P}_{L,M}^{cav}\sin\psi_{in}\right)\hat{X}_M, \tag{SI B.20}$$

where $\Delta = \omega_L - \omega_c$ is the detuning of the laser with respect to the cavity resonance ω_c and g is the light-enhanced optomechanical coupling rate. The cavity linewidth κ has contributions from the the in-and-out-coupling mirror (κ_{in}) – we probe the cavity in reflection – and the highly-reflective (HR) back mirror (κ_{ex}^{HR}) as well as from intracavity losses (κ_{ex}^{loss}), such that $\kappa = \kappa_{in} + \kappa_{ex}$, with $\kappa_{ex} = \kappa_{ex}^{HR} + \kappa_{ex}^{loss}$ where the subscript ex signifies any extra loss mechanism. Losses due to the HR mirror and due to intracavity scattering are mathematically equivalent. Finally, $\psi_{in} = \arctan(2\Delta/\kappa)$ denotes the phase of the intracavity field relative to input field.

The time evolution of the optical and mechanical variables, including decay and fluctuations, is given by the Heisenberg-Langevin equations. In the frequency domain, and in the steady-state regime, the equations of motion are

$$\begin{pmatrix} \kappa/2 - i\Omega & \Delta & 2g\sin\psi_{in} \\ -\Delta & \kappa/2 - i\Omega & -2g\cos\psi_{in} \\ -4g\cos\psi_{in} & -4g\sin\psi_{in} & \chi_{M00}^{-1} \end{pmatrix} \begin{pmatrix} \hat{X}_{L,M}^{cav} \\ \hat{P}_{L,M}^{cav} \\ \hat{X}_M \end{pmatrix} = \begin{pmatrix} \sqrt{\kappa_{in}}\hat{X}_{L,M}^{in} + \sqrt{\kappa_{ex}}\hat{X}_{L,M}^{ex} \\ \sqrt{\kappa_{in}}\hat{P}_{L,M}^{in} + \sqrt{\kappa_{ex}}\hat{P}_{L,M}^{ex} \\ \hat{F}_M \end{pmatrix}, \tag{SI B.21}$$

in which $\chi_{M00}^{-1} \equiv (\omega_{M0}^2 - \Omega^2 - i\Omega\gamma_{M0})/\omega_{M0}$ (the subscript denotes that this susceptibility excludes both dynamical broadening and optical spring effects) and $\hat{X}_{L,M}^{in}$ ($\hat{X}_{L,M}^{ex}$) is the input quantum field leaking in via the port 'in' ('ex'). The port 'in' corresponds to the main in/outcoupler, while mathematically port 'ex' corresponds to both the HR mirror

and intra-cavity loss, which act in the same way since no light is present at the input of HR. The dynamics of the membrane momentum are calculated from the relation $-i\Omega\hat{X}_{\rm M} = \omega_{\rm M0}\hat{P}_{\rm M}$. The natural linewidth of the mechanical mode is $\gamma_{\rm M0}$, and the mean occupation due to the thermal reservoir at temperature T is $n_{\rm M0} = \hbar\omega_{\rm M0}/k_B T$.

We are interested both in the effect of the mechanical mode on the light variables and in the dynamics of the oscillator itself. By defining the matrices

$$\mathbf{A} = \begin{pmatrix} \kappa/2 - i\Omega & \Delta \\ -\Delta & \kappa/2 - i\Omega \end{pmatrix}, \quad \mathbf{B} = \begin{pmatrix} 0 \\ -2g \end{pmatrix}, \quad \mathbf{C} = \begin{pmatrix} -4g & 0 \end{pmatrix}, \quad \hat{\boldsymbol{X}}^{j}_{\rm L,M} = \begin{pmatrix} \hat{X}^{j}_{\rm L,M} \\ \hat{P}^{j}_{\rm L,M} \end{pmatrix}, \tag{SI B.22}$$

$\boldsymbol{O}_{\psi}$ as the input-intracavity field phase rotation (see Eq. (SI B.19)) and the index $j \in \{\text{cav}, \text{in}, \text{ex}\}$ for optical fields, we write Eq. (SI B.21) as system of matrix equations. Noting that the cavity response matrix $\mathbf{A}$ is invariant under quadrature rotations, $\boldsymbol{O}_{\psi}\mathbf{A}\boldsymbol{O}_{\psi}^{\intercal} = \mathbf{A}$, we find the intracavity field and the mechanical variable as a function of the input fluctuations and thermal bath

$$\hat{\boldsymbol{X}}^{\rm cav}_{\rm L,M} = \mathbf{A}^{-1}\left(\sqrt{\kappa_{\rm in}}\hat{\boldsymbol{X}}^{\rm in}_{\rm L,M} + \sqrt{\kappa_{\rm ex}}\hat{\boldsymbol{X}}^{\rm ex}_{\rm L,M}\right) - \mathbf{A}^{-1}\mathbf{O}_{\psi_{\rm in}}\mathbf{B}\hat{X}_{\rm M}, \tag{SI B.23}$$

$$\hat{X}_{\rm M} = \chi_{\rm M}\left[-\mathbf{C}\mathbf{A}^{-1}\mathbf{O}^{\intercal}_{\psi_{\rm in}}\left(\sqrt{\kappa_{\rm in}}\hat{\boldsymbol{X}}^{\rm in}_{\rm L,M} + \sqrt{\kappa_{\rm ex}}\hat{\boldsymbol{X}}^{\rm ex}_{\rm L,M}\right) + \hat{F}_{\rm M}\right], \tag{SI B.24}$$

in which $\chi_{\rm M} = (\chi^{-1}_{\rm M00} - \mathbf{C}\mathbf{A}^{-1}\mathbf{B})^{-1}$ is the effective mechanical susceptibility in the presence of optomechanical coupling. Substituting Eq. (SI B.24) in Eq. (SI B.23) solves the system for the cavity field

$$\hat{\boldsymbol{X}}^{\rm cav}_{\rm L,M} = \mathbf{O}_{\psi_{\rm in}}\mathbf{Y}^{-1}\mathbf{O}^{\intercal}_{\psi_{\rm in}}\left(\sqrt{\kappa_{\rm in}}\hat{\boldsymbol{X}}^{\rm in}_{\rm L,M} + \sqrt{\kappa_{\rm ex}}\hat{\boldsymbol{X}}^{\rm ex}_{\rm L,M}\right) - \mathbf{O}_{\psi_{\rm in}}\mathbf{Y}^{-1}\mathbf{B}\chi_{\rm M00}\hat{F}_{\rm M}, \tag{SI B.25}$$

where $\mathbf{Y} = \mathbf{A} - \mathbf{B}\chi_{\rm M00}\mathbf{C}$ is the effective cavity response matrix in the presence of optomechanical coupling. This quantity can also be used to express the mechanical response (SI B.24) as

$$\hat{X}_{\rm M} = -\chi_{\rm M00}\mathbf{C}\mathbf{Y}^{-1}\mathbf{O}^{\intercal}_{\psi_{\rm in}}\left(\sqrt{\kappa_{\rm in}}\hat{\boldsymbol{X}}^{\rm in}_{\rm L,M} + \sqrt{\kappa_{\rm ex}}\hat{\boldsymbol{X}}^{\rm ex}_{\rm L,M}\right) + \chi_{\rm M}\hat{F}_{\rm M}. \tag{SI B.26}$$

Finally, we detect the reflected field off port 1 in a homodyne measurement. The phase of the outgoing classical carrier field with respect to the cavity field is given by $\psi_{\rm out} = \arctan(2\Delta/(\kappa_{\rm in} - \kappa_{\rm ex}))$. Overall, the total phase shift with respect to the input field is $\psi_{\rm out} + \psi_{\rm in}$. The cavity input-output relations, taking account for the acquired phase shift with respect to the input, from Eq. (SI B.25), is

$$\begin{aligned}\hat{\boldsymbol{X}}^{\rm out}_{\rm L,M} &= \mathbf{O}^{\intercal}_{\psi_{\rm in}+\psi_{\rm out}}(-\hat{\boldsymbol{X}}^{\rm in}_{\rm L,M} + \sqrt{\kappa_{\rm in}}\hat{\boldsymbol{X}}^{\rm cav}_{\rm L,M}) \\ &= \mathbf{O}^{\intercal}_{\psi_{\rm out}}(\kappa_{\rm in}\mathbf{Y}^{-1} - \mathbf{1}_2)\mathbf{O}^{\intercal}_{\psi_{\rm in}}\hat{\boldsymbol{X}}^{\rm in}_{\rm L,M} + \sqrt{\kappa_{\rm in}\kappa_{\rm ex}}\mathbf{O}^{\intercal}_{\psi_{\rm out}}\mathbf{Y}^{-1}\mathbf{O}^{\intercal}_{\psi_{\rm in}}\hat{\boldsymbol{X}}^{\rm ex}_{\rm L,M} - \sqrt{\kappa_{\rm in}}\mathbf{O}^{\intercal}_{\psi_{\rm out}}\mathbf{Y}^{-1}\mathbf{B}\chi_{\rm M00}\hat{F}_{\rm M},\end{aligned} \tag{SI B.27}$$

where in the second line we have substituted the solution for the intracavity field (SI B.25).

Above we have developed the exact Fourier-domain solution to a (linearised) cavity-optomechanical system, in particular the mechanical response (SI B.24) and the optomechanical input-output relation (SI B.23). We now derive the simplified versions of these equations used in the main text to emphasise the essential physics of our scheme. We note that the cavity response matrix can be expressed in terms of the complex Lorentzian sideband amplitudes $\mathcal{L}(\Omega) \equiv (\kappa/2)/[\kappa/2 - i(\Omega + \Delta)]$ with phase $\Theta(\Omega) \equiv \text{Arg}[\mathcal{L}(\Omega)]$ as

$$\mathbf{A}^{-1} = \frac{1}{\kappa}\begin{pmatrix} \mathcal{L}(\Omega) + \mathcal{L}^*(-\Omega) & i[\mathcal{L}(\Omega) - \mathcal{L}^*(-\Omega)] \\ -i[\mathcal{L}(\Omega) - \mathcal{L}^*(-\Omega)] & \mathcal{L}(\Omega) + \mathcal{L}^*(-\Omega) \end{pmatrix} \tag{SI B.28}$$

$$= \frac{|\mathcal{L}(\Omega)| + |\mathcal{L}(-\Omega)|}{\kappa} e^{i[\Theta(\Omega) - \Theta(-\Omega)]/2}\mathbf{O}_{[\Theta(\Omega)+\Theta(-\Omega)]/2}\left[\mathbf{1}_2 + i\frac{|\mathcal{L}(\Omega)| - |\mathcal{L}(-\Omega)|}{|\mathcal{L}(\Omega)| + |\mathcal{L}(-\Omega)|}\mathbf{O}_{-\pi/2}\right]. \tag{SI B.29}$$

Assuming that the dependence of $\mathcal{L}(\Omega)$ on the Fourier frequency Ω is negligible over the bandwidth of interest, we may approximate $\mathcal{L}(\pm\Omega) \approx \mathcal{L}(\pm\omega_{\rm M})$ (and accordingly $\Theta(\pm\Omega) \approx \Theta(\pm\omega_{\rm M})$). Within this approximation, we can achieve the simplified mechanical response and input-output equations employed in the main text by introducing the rotated quadrature basis

$$\boldsymbol{X}^{\text{in(ex)}\prime}_{\rm L,M} \equiv e^{i[\Theta(\omega_{\rm m}) - \Theta(-\omega_{\rm m})]/2}\mathbf{O}_{[\Theta(\omega_{\rm m})+\Theta(-\omega_{\rm m})]/2}\mathbf{O}^{\intercal}_{\psi_{\rm in}}\boldsymbol{X}^{\text{in(ex)}}_{\rm L,M}. \tag{SI B.30}$$

In this way, using Eqs. (SI B.29) and (SI B.30) to reexpress the QBA force on the mechanical mode (i.e., Eq. (SI B.24), 1st term in square brackets), we find

$$-\mathbf{C}\mathbf{A}^{-1}\mathbf{O}^{\intercal}_{\psi_{\rm in}}\left(\sqrt{\kappa_{\rm in}}\hat{\boldsymbol{X}}^{\rm in}_{\rm L,M} + \sqrt{\kappa_{\rm ex}}\hat{\boldsymbol{X}}^{\rm ex}_{\rm L,M}\right) \approx 2\sqrt{\Gamma_{\rm M}}\begin{pmatrix} 1 \\ i\zeta_{\rm M} \end{pmatrix}^{\intercal}\left(\sqrt{\kappa_{\rm in}/\kappa}\hat{\boldsymbol{X}}^{\rm in\prime}_{\rm L,M} + \sqrt{\kappa_{\rm ex}/\kappa}\hat{\boldsymbol{X}}^{\rm ex\prime}_{\rm L,M}\right), \tag{SI B.31}$$

where we have introduced the mechanical readout rate and sideband asymmetry parameter,

$$\Gamma_{\rm M} \equiv \frac{4g^2}{\kappa}(|\mathcal{L}(\omega_{\rm M})| + |\mathcal{L}(-\omega_{\rm M})|)^2, \quad \zeta_{\rm M} \equiv \frac{|\mathcal{L}(\omega_{\rm M})| - |\mathcal{L}(-\omega_{\rm M})|}{|\mathcal{L}(\omega_{\rm M})| + |\mathcal{L}(-\omega_{\rm M})|}, \tag{SI B.32}$$

respectively. Finally, we ignore the finite cavity overcoupling by setting $\kappa_{\rm in} = \kappa$ (and hence $\kappa_{\rm ex} = 0$) in Eq. (SI B.31) to arrive at the main-text expression for the response of $\hat{X}_{\rm M}$. Noting that $-\mathbf{1}_2 + \kappa\mathbf{A}^{-1} = e^{i[\Theta(\omega_{\rm m})-\Theta(-\omega_{\rm m})]}\mathbf{O}_{\Theta(\omega_{\rm m})+\Theta(-\omega_{\rm m})}$, we find in the same limit that the rotated output quadrature

$$\boldsymbol{X}^{\rm out\prime}_{\rm L,M} \equiv e^{-i[\Theta(\omega_{\rm M})-\Theta(-\omega_{\rm M})]/2}\mathbf{O}^{\intercal}_{[\Theta(\omega_{\rm M})+\Theta(-\omega_{\rm M})]/2}\mathbf{O}^{\intercal}_{\psi_{\rm in}}\boldsymbol{X}^{\rm out}_{\rm L,M}, \tag{SI B.33}$$

obeys

$$\boldsymbol{X}^{\rm out\prime}_{\rm L,M} = \boldsymbol{X}^{\rm in\prime}_{\rm L,M} + \sqrt{\Gamma_{\rm M}}\begin{pmatrix} i\zeta_{\rm M} \\ 1 \end{pmatrix}\hat{X}_{\rm M}, \tag{SI B.34}$$

as follows from $\hat{\boldsymbol{X}}^{\rm out}_{\rm L,M} = -\hat{\boldsymbol{X}}^{\rm in}_{\rm L,M} + \sqrt{\kappa_{\rm in}}\hat{\boldsymbol{X}}^{\rm cav}_{\rm L,M}$ combined with Eq. (SI B.23), again assuming $\kappa_{\rm in} = \kappa$. Dropping the primes on the quadrature variables in Eq. (SI B.34) for brevity we arrive at the input-output relation presented in the main text.

3. Hybrid system I/O relations

The subsystems are coupled following the relation

$$\hat{\boldsymbol{X}}^{\rm in}_{\rm L,M} = \mathbf{O}_{\varphi}(\sqrt{\nu}\hat{\boldsymbol{X}}^{\rm out}_{\rm L,S} + \sqrt{1-\nu}\hat{\boldsymbol{X}}_{\rm L,\nu}), \tag{SI B.35}$$

where optical transmission losses between the systems are modelled as a beam splitter with power transmission ν, and $\hat{\boldsymbol{X}}^{\rm out}_{\rm L,S}$ is defined Eq. (SI B.14). In general, the mechanical oscillator is not only coupled to light and its own thermal bath, but effectively also to the spin oscillator

$$\hat{X}_{\rm M} = -\chi_{\rm M00}\mathbf{C}\mathbf{Y}^{-1}\mathbf{O}^{\intercal}_{\psi_{\rm in}}\left(\sqrt{\nu\kappa_{\rm in}}\mathbf{O}_{\varphi}[(\mathbf{1}_2 + 2\Gamma_{\rm S}\mathbf{Z}\mathbf{L}\mathbf{Z})\hat{\boldsymbol{X}}^{\rm in}_{\rm L,S} + \sqrt{\Gamma_{\rm S}}\mathbf{Z}\mathbf{L}\hat{\boldsymbol{F}}_{\rm S}] + \sqrt{(1-\nu)\kappa_{\rm in}}\mathbf{O}_{\varphi}\hat{\boldsymbol{X}}_{\rm L,\nu} + \sqrt{\kappa_{\rm ex}}\hat{\boldsymbol{X}}^{\rm ex}_{\rm L,M}\right)$$
$$+ (\chi^{-1}_{\rm M00} - \mathbf{C}\mathbf{A}^{-1}\mathbf{B})^{-1}\hat{F}_{\rm M}, \tag{SI B.36}$$

as follows by combining Eqs. (SI B.26), (SI B.35), and (SI B.14). At the output of the optical cavity, the field is homodyned at a quadrature of choice defined by the phase ϑ, $\hat{\boldsymbol{X}}^{\rm meas}_{\rm L} = \sqrt{\eta}\mathbf{O}_{\vartheta}\hat{\boldsymbol{X}}^{\rm out}_{\rm L,M} + \sqrt{1-\eta}\hat{\boldsymbol{X}}_{\rm L,\eta}$, accounting for mode-matching and optical losses on the way to the final detector by the efficiency η. The detected field, including all contributions from losses, rotations and oscillator couplings is

$$\hat{\boldsymbol{X}}^{\rm meas}_{\rm L} = \sqrt{\eta}\mathbf{O}_{\vartheta}\mathbf{O}^{\intercal}_{\psi_{\rm out}}(\kappa_{\rm in}\mathbf{Y}^{-1} - \mathbf{1}_2)\mathbf{O}^{\intercal}_{\psi_{\rm in}}\left(\sqrt{\nu}\mathbf{O}_{\varphi}[(\mathbf{1}_2 + 2\Gamma_{\rm S}\mathbf{Z}\mathbf{L}\mathbf{Z})\hat{\boldsymbol{X}}^{\rm in}_{\rm L,S} + \sqrt{\Gamma_{\rm S}}\mathbf{Z}\mathbf{L}\hat{\boldsymbol{F}}_{\rm S}] + \sqrt{1-\nu}\mathbf{O}_{\varphi}\hat{\boldsymbol{X}}_{\rm L,\nu}\right)$$
$$+ \sqrt{\eta\kappa_{\rm in}\kappa_{\rm ex}}\mathbf{O}_{\vartheta}\mathbf{O}^{\intercal}_{\psi_{\rm out}}\mathbf{Y}^{-1}\mathbf{O}^{\intercal}_{\psi_{\rm in}}\hat{\boldsymbol{X}}^{\rm ex}_{\rm L,M} - \sqrt{\eta\kappa_{\rm in}}\mathbf{O}_{\vartheta}\mathbf{O}^{\intercal}_{\psi_{\rm out}}\mathbf{Y}^{-1}\mathbf{B}\chi_{\rm M00}\hat{F}_{\rm M} + \sqrt{1-\eta}\hat{\boldsymbol{X}}_{\rm L,\eta}. \tag{SI B.37}$$

Note that the homodyne measurement only allows us to access one component of $\hat{\boldsymbol{X}}^{\rm meas}_{\rm L}$ for a given choice of ϑ.

The equations (SI B.13), (SI B.36), and (SI B.37) contain the full information needed to fit the experimental data and quantify correlations among the various constituents. To ease the handling of the theory, we construct a rectangular transformation matrix $\mathbf{U}$ in the input basis of the forces acting on the systems $\boldsymbol{Q}_{\rm in} \equiv (\hat{F}^X_{\rm S}, \hat{F}^P_{\rm S}, \hat{F}_{\rm M}, \hat{X}^{\rm in}_{\rm L,S}, \hat{P}^{\rm in}_{\rm L,S}, \hat{X}^{\rm in}_{\rm L,\nu}, \hat{P}^{\rm in}_{\rm L,\nu}, \hat{X}^{\rm in}_{\rm L,ex}, \hat{P}^{\rm in}_{\rm L,ex}, \hat{X}^{\rm in}_{\rm L,\eta}, \hat{P}^{\rm in}_{\rm L,\eta})^{\intercal}$ such that

$$\boldsymbol{Q}_{\rm out} = \mathbf{U}\boldsymbol{Q}_{\rm in} \tag{SI B.38}$$

and the output basis $\boldsymbol{Q}_{\rm out} \equiv (\hat{X}_{\rm M}, \hat{P}_{\rm M}, \hat{X}_{\rm S}, \hat{P}_{\rm S}, \hat{P}^{\rm meas}_{\rm L})^{\intercal}$, which are all the output operators we might potentially be interested in.

The various power (and cross) spectral densities are calculated by taking the absolute square of the vector $\boldsymbol{Q}_{\rm out}$ given the input matrix of spectral densities

$$\bar{\mathbf{S}}_{\rm in}\delta(\Omega - \Omega') = \frac{1}{2}\langle\boldsymbol{Q}^{\dagger}_{\rm in}(\Omega)[\boldsymbol{Q}_{\rm in}(\Omega')]^{\intercal} + \boldsymbol{Q}_{\rm in}(\Omega)[\boldsymbol{Q}^{\dagger}_{\rm in}(\Omega')]^{\intercal}\rangle, \tag{SI B.39}$$

where $\intercal$ signifies a row-vector, while $\dagger$ indicates Hermitian conjugation of the individual vector elements, not the vector as a whole. $\bar{\mathbf{S}}_{\text{in}}$ is a square matrix with diagonal entries

$$\text{diag}(\bar{\mathbf{S}}_{\text{in}}) = \left(\overline{S}_{F_{\text{S}}^X F_{\text{S}}^X}, \overline{S}_{F_{\text{S}}^P F_{\text{S}}^P}, \overline{S}_{F_{\text{M}} F_{\text{M}}}, \overline{S}_{X_{\text{L}} X_{\text{L}}}, \overline{S}_{P_{\text{L}} P_{\text{L}}}, \overline{S}_{X_{\text{L}} X_{\text{L}}}, \overline{S}_{P_{\text{L}} P_{\text{L}}} + \frac{\nu}{1-\nu}\overline{S}_{\text{S,bb}}, \overline{S}_{X_{\text{L}} X_{\text{L}}}, \overline{S}_{P_{\text{L}} P_{\text{L}}}, \overline{S}_{X_{\text{L}} X_{\text{L}}}, \overline{S}_{P_{\text{L}} P_{\text{L}}}\right), \tag{SI B.40}$$

and all other elements equal to zero. Notably, for an easier theoretical treatment, the broadband noise is added via the inter-system loss port in the $\hat{P}^{\text{in}}_{\text{L},\nu}$ field. As defined above, it effectively experiences the same losses and rotation as the narrowband atomic noise. The various power spectral densities above are defined in equations (SI B.6) and (SI B.7), with Fourier frequency dependencies Ω dropped for brevity. The diagonal entries related to light variables are all vacuum, therefore the indistinguishable labelling.

This allows us to calculate the spectral densities of the output signals as follows

$$\bar{\mathbf{S}}_{\text{out}} = \mathbf{U}^\dagger \bar{\mathbf{S}}_{\text{in}} \mathbf{U}, \tag{SI B.41}$$

where $\mathbf{U}^\dagger$ is conjugate-transpose matrix w.r.t. to $\mathbf{U}$. For instance, the (1,1) element of $\bar{\mathbf{S}}_{\text{out}}$ is the power spectral density of the mechanical oscillator position $\bar{S}_{X_{\text{M}} X_{\text{M}}}$.

We may now calculate the steady-state unconditional covariance matrix in the spin-mechanics subspace. For this we integrate $\bar{\mathbf{S}}_{\text{MS}}$, which we define as the submatrix of $\bar{\mathbf{S}}_{\text{out}}$ containing the first 4 rows and columns, leading to the unconditional covariance matrix

$$\mathbf{V}_u = \int_{-\infty}^{\infty} \frac{\mathrm{d}\Omega}{2\pi} \bar{\mathbf{S}}_{\text{MS}}(\Omega). \tag{SI B.42}$$

Figures SI5a, SI6a, and SI7a present examples of $\mathbf{V}_u$ in different cases and bases.

Appendix C: Wiener filtering

In this Appendix we detail the central concepts of the conditional quantum state and the Wiener filtering procedure employed to extract conditional expectation values from measurement data.

A strong projective measurement of the initial system state $\hat{\rho}$ with a set of measurement operators $\{\hat{\Pi}_i\}$ generates a conditional quantum state $\hat{\rho}_c = \hat{\Pi}_i \hat{\rho} \hat{\Pi}_i / \text{Tr}(\hat{\Pi}_i \hat{\rho} \hat{\Pi}_i)$. In a quasi-continuous (multi-step) weak measurement, we replace the projection operators with a set of generalised measurement operators (positive operator-valued measures) acting repeatedly on the initial state [13, 14]. In general, prediction of the conditional state would require knowledge of operators associated with each measured value. For Gaussian states, the situation simplifies so that a linear, stationary filter can be used.

Given the weak, continuous character of our optical probing, useful measurement results must necessarily be obtained as (weighted) averages over finite segments of the homodyne measurement current. The appropriate temporal filter functions are defined by the system evolution during probing and the meter noise characteristics, necessitating precise knowledge of the equations of motion and the input-output relations. The methodology outlined here is known in classical physics and engineering as Kalman filtering, and its applicability to Gaussian quantum systems was proven in Refs. [15, 16] in a manner that we will now describe.

We note that our optical probing has the following two "classical" properties: First, the operators associated with the measurement current obtained at different times t and t' commute, $[\hat{P}^{\text{out}}_{\text{L}}(t), \hat{P}^{\text{out}}_{\text{L}}(t')] = 0$, implying their *simultaneous measurability*; second, causality entails that the measurement current at a given time t does not respond to the future system evolution (at times $t' > t$), in turn leading to the property $[\hat{P}^{\text{out}}_{\text{L}}(t), \hat{X}(t')] = 0$, $t' > t$, with $\hat{X}$ being any quadrature of a hybrid spin-mechanics system. Hence, the only manifestation of quantum mechanics in our probing scheme is that it enforces the presence of amplitude and phase (quantum) noise in the meter field according to the Heisenberg uncertainty relation. As the microscopic origin of the noise is immaterial to (classical) Wiener filtering theory, it follows from the above observations that it is applicable to our Gaussian quantum system.

As necessary prerequisites we introduce the PSD of the measurement current as $\bar{S}_{ii} \equiv \bar{S}_{P_{\text{L}}^{\text{meas}} P_{\text{L}}^{\text{meas}}}$ since $i(t)$ is the result of a quadrature measurement. In general, we aim to track the entire hybrid system characterised by $\boldsymbol{Q} = (\hat{X}_{\text{M}}, \hat{P}_{\text{M}}, \hat{X}_{\text{S}}, \hat{P}_{\text{S}})^\intercal$. Furthermore, we need to consider the signal-current correlation (cross-spectral density) row vector $\bar{\mathbf{S}}_{\boldsymbol{Q}i}$, which is the last row of $\bar{\mathbf{S}}_{\text{out}}$, Eq. (SI B.41). The spectral densities $\bar{S}(\Omega)$ are used to compute temporal correlation functions $\bar{C}(\tau)$ using the inverse Fourier transform thanks to the Wiener-Khinchin theorem.

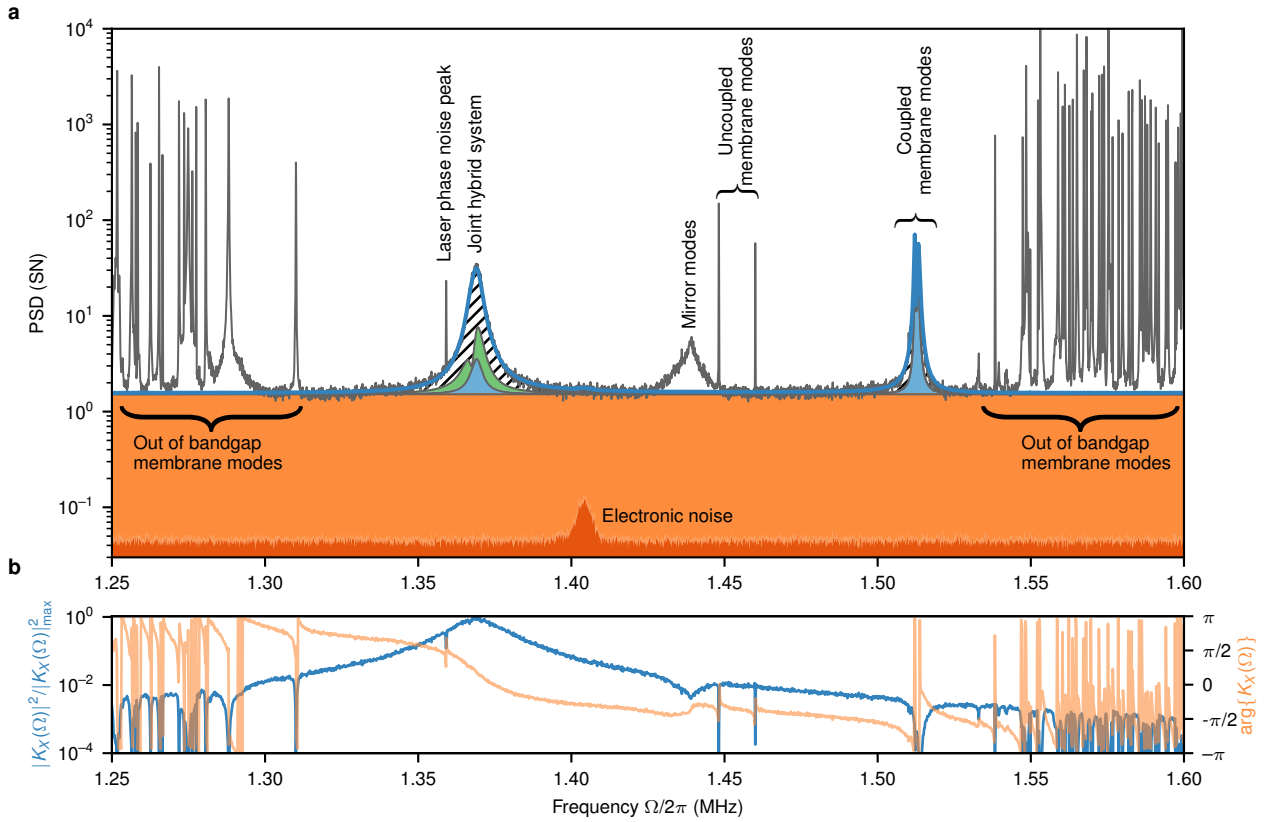

Figure SI4. **Spectra from Fig. 3b and associated Wiener filter from Fig. 3c shown in a wider range. a,** the spectrum is again decomposed into the same components as in Fig. 3b, yet including the electronic detection noise (dark orange). Furthermore, additional membrane modes are visible in the experimental data. We model two of those modes, around 1.52 MHz, including their back-action. Those are the only high-Q modes in the bandgap that are significantly coupled to light, which stretches from 1.31 to 1.54 MHz. Notably, the additional modes are treated as noise in the process of detecting the motion of the main defect mode of interest and the motion of spins. **b,** Wiener filter for the hybrid EPR system (squared normalised amplitude, left axis, phase, right axis). The filter automatically allows efficient tracking of the main EPR signal with other sources of noise removed in the form of frequency notch filters. Notably, the Wiener filter is significantly broader than the linewidth of the system itself.

Our hybrid system is driven solely by optical and thermal forces with wide-sense stationary noise statistics (i.e., constant first and second moments of all noises, and all covariances depending only on the time difference $t - t'$) [17]. Under these circumstances the appropriate set of causal filters $\mathbf{K}$ for purposes of estimating the system first and second moments is the so-called *Wiener filter* [18]. Convolving the filter with the measurement current yields the best unbiased estimate of the system variables (i.e., with the minimum mean-square error):

$$\boldsymbol{Q}^c_\infty(t) = \int_{-\infty}^{t} \mathbf{K}(t'-t) i(t')\,\mathrm{d}t', \tag{SI C.1}$$

where $\boldsymbol{Q}^c = (X^c_\mathrm{M}, P^c_\mathrm{M}, X^c_\mathrm{S}, P^c_\mathrm{S})^\intercal$ is the conditional trajectory in the steady-state scenario, i.e., for the case where we have $i(t)$ for all previous times available. In a more general case, where upon conditioning we increase the length of past data, we generally write:

$$\boldsymbol{Q}^c(t) = \int_{0}^{t} \mathbf{K}(t'-t, t) i(t')\,\mathrm{d}t', \tag{SI C.2}$$

where $\mathbf{K}(\tau, t)$ is the filter function, t' is the running argument of convolution and t is the length of the conditioning interval.

To find the Wiener filters $\mathbf{K}$, we solve the Wiener-Hopf equations, which state that the optimal $\boldsymbol{Q}^c(t)$ must obey

$$\bar{\mathbf{C}}_{\boldsymbol{Q}^c i}(t') = \bar{\mathbf{C}}_{\boldsymbol{Q} i}(t'), \tag{SI C.3}$$

for all t' within the conditioning window. In the limit of infinite conditioning time, the Wiener-Hopf equation (SI C.3) is typically stated as

$$\int_0^\infty \mathbf{K}^\intercal(-t'')\bar{C}_{ii}(t'-t'')\,\mathrm{d}t'' = \bar{\mathbf{C}}_{\boldsymbol{Q} i}(t') \quad \forall\, t' \geq 0, \tag{SI C.4}$$

where $\bar{\mathbf{C}}_{\boldsymbol{Q} i}(t')$ is the cross-correlation between $\boldsymbol{Q}$ and i calculated as the inverse Fourier transform of $\bar{\mathbf{S}}_{\boldsymbol{Q} i}(\Omega)$, which is a row vector of cross-spectral densities (first four elements of the last row of $\bar{\mathbf{S}}_{\mathrm{out}}$, Eq. (SI B.41)). The vector form of the above equation should here be understood as 4 independent equations.

If we only have data available for a finite past, we limit the above infinite integral to t and find the finite-input response filter $\mathbf{K}(t', t)$ as a solution of

$$\int_0^t \mathbf{K}^\intercal(-t'', t)\bar{C}_{ii}(t'-t'')\,\mathrm{d}t'' = \bar{\mathbf{C}}_{\boldsymbol{Q} i}(t') \quad \forall\, t' \in [0, t]. \tag{SI C.5}$$

In this form, the Wiener-Hopf equation can also be easily discretised and cast in a matrix equation form. The solution is then obtained via the Levinson–Durbin recursion algorithm. It is noteworthy that in the finite-time limit, the Wiener filter $\mathbf{K}(t', t)$ is only defined for $-t < t' < 0$, in accordance with the integration domain in Eq. (SI C.2).

While the trajectory $\boldsymbol{Q}^c$ is stochastic, the variance of residual fluctuations is deterministic; it can be calculated as the difference between the *unconditional* covariance matrix $\mathbf{V}_u$ and the (ensemble) covariance matrix of the best estimates $\mathbf{V}_{\mathrm{be}}$,

$$\mathbf{V}_c = \mathbf{V}_u - \mathbf{V}_{\mathrm{be}}, \tag{SI C.6}$$

where

$$\mathbf{V}_{\mathrm{be}} = \int_0^\infty \mathbf{K}(-t)\bar{\mathbf{C}}_{\boldsymbol{Q} i}(t)\,\mathrm{d}t = \mathrm{Cov}(\boldsymbol{Q}, \boldsymbol{Q}^c_\infty), \tag{SI C.7}$$

is the 4 by 4 covariance matrix of the best estimates and $\boldsymbol{Q}^c(t)$ is given by Eq. (SI C.1). In the case of a finite conditioning interval, we again limit the integration:

$$\mathbf{V}_{\mathrm{be}}(t) = \int_0^t \mathbf{K}(-t', t)\bar{\mathbf{C}}_{\boldsymbol{Q} i}(t')\,\mathrm{d}t' = \mathrm{Cov}(\boldsymbol{Q}, \boldsymbol{Q}^c(t)), \tag{SI C.8}$$

where $\boldsymbol{Q}^c(t)$ is defined by Eq. (SI C.2). Again, Eq. (SI C.6) holds, and hence captures how the conditional variance evolves as we increase the conditioning time t. The relation $\mathbf{V}_{\mathrm{be}}(t) = \mathrm{Cov}(\boldsymbol{Q}, \boldsymbol{Q}^c(t))$ implied by Eq. (SI C.8) follows directly from the Wiener-Hopf equation (SI C.3) by convolving it with $\mathbf{K}$ (as does the special case (SI C.7)).

We present the obtained Wiener filter, for the point with best entanglement (see SI D), in Fig. 3 of the main text, and for a wider frequency range in Fig. SI4. The time evolution of the conditional variance is shown in Fig. 1, and the final V_{c} is shown in Fig. 4.

Finally, it is noteworthy that the Wiener filter shares many characteristics with the widely used Kalman filter. In fact, the Wiener filter is a specific case of a Kalman filter where it can be obtained from the Wiener-Hopf equations since both noise and signal are wide-sense stationary. This still applies to our case of a finite-input response filter $\mathbf{K}(t', t)$, as to find it we assume stationary noise. In fact, the finite-input response (FIR) Wiener filters are widely used in engineering contexts. In a more general case one needs to solve Kalman equations that are qualitatively different.

Appendix D: Entanglement estimation

Let us now analyse the properties of the covariance matrices, obtained using the hybrid system model (SI B) and Wiener filtering (SI C), and estimate the entanglement of the bipartite state. In Fig. SI5(a) the covariance matrix $\mathbf{V}_u$ corresponding to the case with best entanglement is presented. Diagonal elements represent the occupations of individual oscillators. The conditioning procedure is then applied to obtain $\mathbf{V}_c$ in Fig. SI5(b). Notably, we observe strong positive correlation between $\hat{X}_{\mathrm{M}}$ and $\hat{X}'_{\mathrm{S}}$ as well as negative correlation between $\hat{P}_{\mathrm{M}}$ and $\hat{P}'_{\mathrm{S}}$. Furthermore,

we can see that the conditioning procedure mostly allow us to decrease the conditional occupation of the mechanical subsystem, which is most efficiently measured. The spin variables here are rotated, i.e., $\hat{X}'_{\rm S} = \hat{X}_{\rm S}\cos\beta + \hat{P}_{\rm S}\sin\beta$, $\hat{P}'_{\rm S} = \hat{P}_{\rm S}\cos\beta - \hat{X}_{\rm S}\sin\beta$ such the anti-diagonal of $\mathbf{V}_c$ is nulled.

The estimation of the best entangled state involves the construction the general EPR variables

$$\hat{X}_{\rm EPR} = (\hat{X}_{\rm M} - a\hat{X}'_{\rm S})/\sqrt{1+a^2} = \boldsymbol{u}_X^{\intercal}\boldsymbol{Q}, \tag{SI D.1}$$

$$\hat{P}_{\rm EPR} = (\hat{P}_{\rm M} + a\hat{P}'_{\rm S})/\sqrt{1+a^2} = \boldsymbol{u}_P^{\intercal}\boldsymbol{Q}, \tag{SI D.2}$$

$$\hat{\boldsymbol{X}}_{\rm EPR} = \mathbf{u}^{\intercal}\boldsymbol{Q} \tag{SI D.3}$$

(with matrix $\mathbf{u}$ having vectors $\boldsymbol{u}_X$ and $\boldsymbol{u}_P$ as columns) along with canonically conjugated variables

$$\hat{X}'_{\rm EPR} = (\hat{X}_{\rm M} + a\hat{X}'_{\rm S})/\sqrt{1+a^2} \tag{SI D.4}$$

$$\hat{P}'_{\rm EPR} = (\hat{P}_{\rm M} - a\hat{P}'_{\rm S})/\sqrt{1+a^2} \tag{SI D.5}$$

where a is the relative weight of the spin component with respect to mechanics and β is the rotation angle of the spin component, and $\boldsymbol{u}_X$ and $\boldsymbol{u}_P$ are unit-length vectors. The EPR variance (conditional or unconditional) $V = \mathrm{Var}[\hat{X}_{\rm EPR}] + \mathrm{Var}[\hat{P}_{\rm EPR}]$ is evaluated using the covariance matrix $\mathbf{V}$ as

$$V_{a,\beta} = \boldsymbol{u}_X^{\intercal}\mathbf{V}\boldsymbol{u}_X + \boldsymbol{u}_P^{\intercal}\mathbf{V}\boldsymbol{u}_P. \tag{SI D.6}$$

For the present data, $a \approx 0.85$, which is approximately constant for all data point, and $\beta \approx 20°$ for the point of best entanglement. For different spin-mechanics detuning optimal β varies by tens of degrees. We have minimised the EPR variance $V = \min_{a,\beta} V_{a,\beta}$ for both parameters individually for each dataset.

Having defied the EPR basis we can now also plot the same matrix as in Fig. SI5 in the new basis, see Fig. SI6. Here, we observe that for $\mathbf{V}_c$ the variance of the EPR components on the diagonal indeed reaches below the classical limit of 0.5.

Finally, we compared the entangled case with the far-detuned case, presented in Fig. SI7. Here we observe negligible off-diagonal correlation terms, and also significantly lower unconditional occupation for mechanics, as it is not driven by the spin noise. Furthermore, the conditioning procedure can now distinguish the systems and efficiently brings down their respective conditional variances.

To generate the conditional trajectory in Fig. 1(c) we first solve Eq. (SI C.5) for a set of conditioning times t and find a collection of Wiener filters $\mathbf{K}(t', t)$. We then use the filters to get $\boldsymbol{Q}^c(t)$ as given by Eq. (SI C.2) as well as conditional covariance matrices $\mathbf{V}_c(t)$ (see Eqs. (SI C.6) and (SI C.8)). We then find the optimal a and β for the $\mathbf{V}_c$ associated with $t \to \infty$, which gives us $\mathbf{u}$. Subsequently, $\boldsymbol{X}^c_{\rm EPR} = \mathbf{u}^{\intercal}\boldsymbol{Q}^c$ is calculated. Finally we move to a rotating frame by $\bar{\boldsymbol{X}}^c_{\rm EPR} = \mathbf{O}_{\omega t}\boldsymbol{X}^c_{\rm EPR}$ with $\omega/2\pi = 1.37\,\mathrm{MHz}$, which is rather an arbitrary choice since for the EPR oscillator there is no single distinguished frequency unless $\omega_{\rm M} = |\omega_{\rm S}|$ exactly, which is not the case.

We observe $\mathrm{Var}[\hat{X}] \approx \mathrm{Var}[\hat{P}]$ for all cases (Figs. SI5–SI7) consistent with our system operating within the regime of validity for the Rotating Wave Approximation.

Appendix E: Uncertainties

We apply elaborate statistical techniques to deduce the statistical uncertainty for the value of the degree of entanglement.

Spectra corresponding to points in Fig. 4b are fitted collectively to the same model. A subset of the parameters is shared between all spectra, while others are allowed to fluctuate from spectrum to spectrum, representing small short-timescale fluctuations.

The parameters that are allowed to change from spectrum to spectrum are atomic frequency, LO_1+LO_2 phase φ, cavity detuning Δ, and mechanical coupling rate g. The drift of the latter two can be explained by a spurious interference, which turns drifts in φ into drifts in optical power in LO_2, which in turns leads to a change in Δ and thus also g. The typical size of drifts of φ is ~ 3 degrees.

We establish prior probabilities for all parameters by independent measurements and calibrations, many of which we explain above. We use those priors for our parameters, together with the spectra and their statistical uncertainties to perform a log-likelihood optimisation. We use Gaussian priors for the parameters and assume a relative Gaussian error of 8 %, stemming from the number of samples for each spectrum $N_{\rm samp} = 200$, i.e., the statistical variance of the

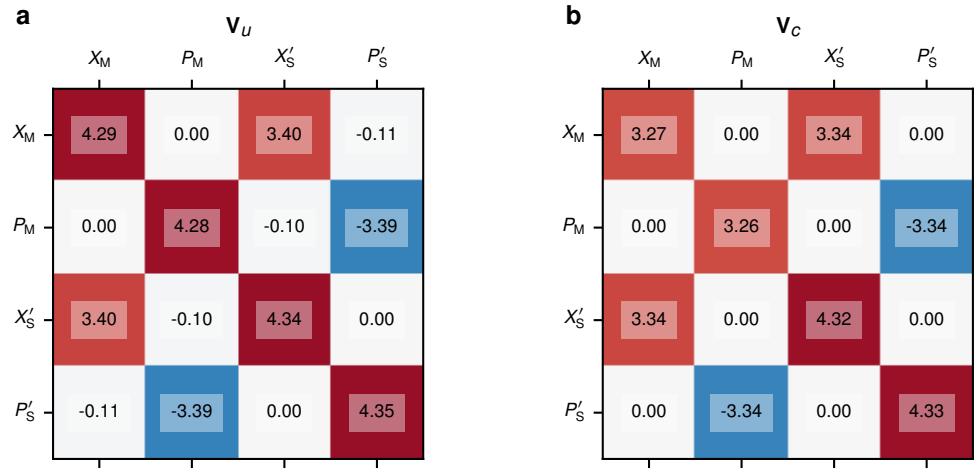

Figure SI5. **Covariance matrices in the individual single-system basis**, for the dataset with $|\omega_S| - \omega_M \approx -\gamma_M/2$. Angle β is adjusted so that anti-diagonal in **b** is 0. **a,** Unconditional and **b,** conditional covariance matrices.

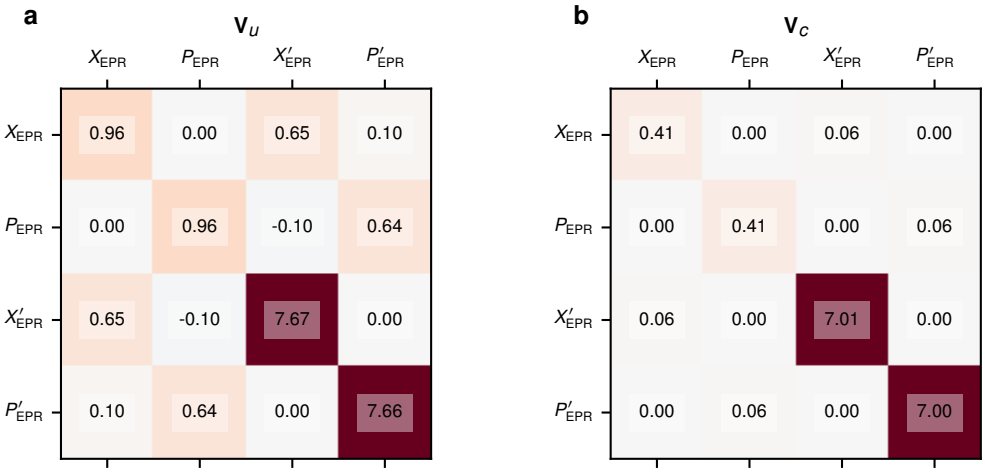

Figure SI6. **Covariance matrices in the EPR basis**, for the dataset with $|\omega_S| - \omega_M \approx -\gamma_M/2$. **a,** Unconditional and **b,** conditional covariance matrices.

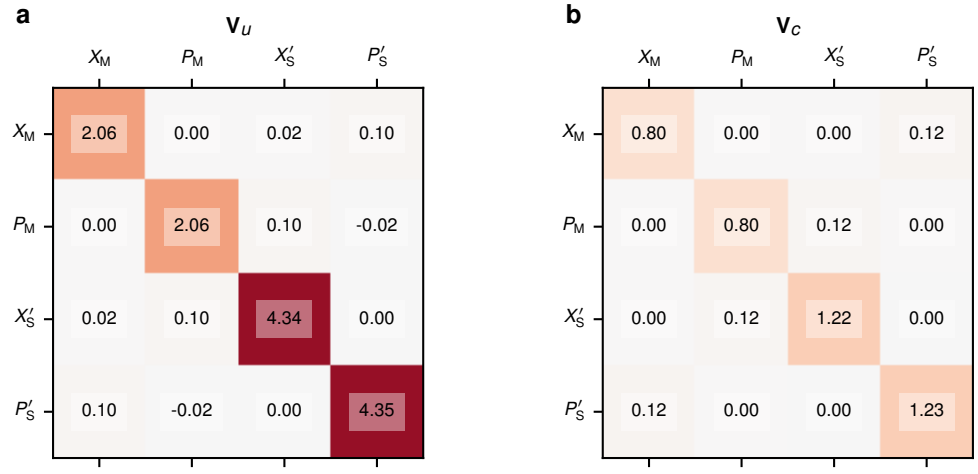

Figure SI7. T**he covariance matrices in the detuned case**, expressed in the individual system basis. Same rotation angle β as in Fig. SI5 for the atomic subsystem is applied here. **a,** Unconditional and **b,** conditional covariance matrices.

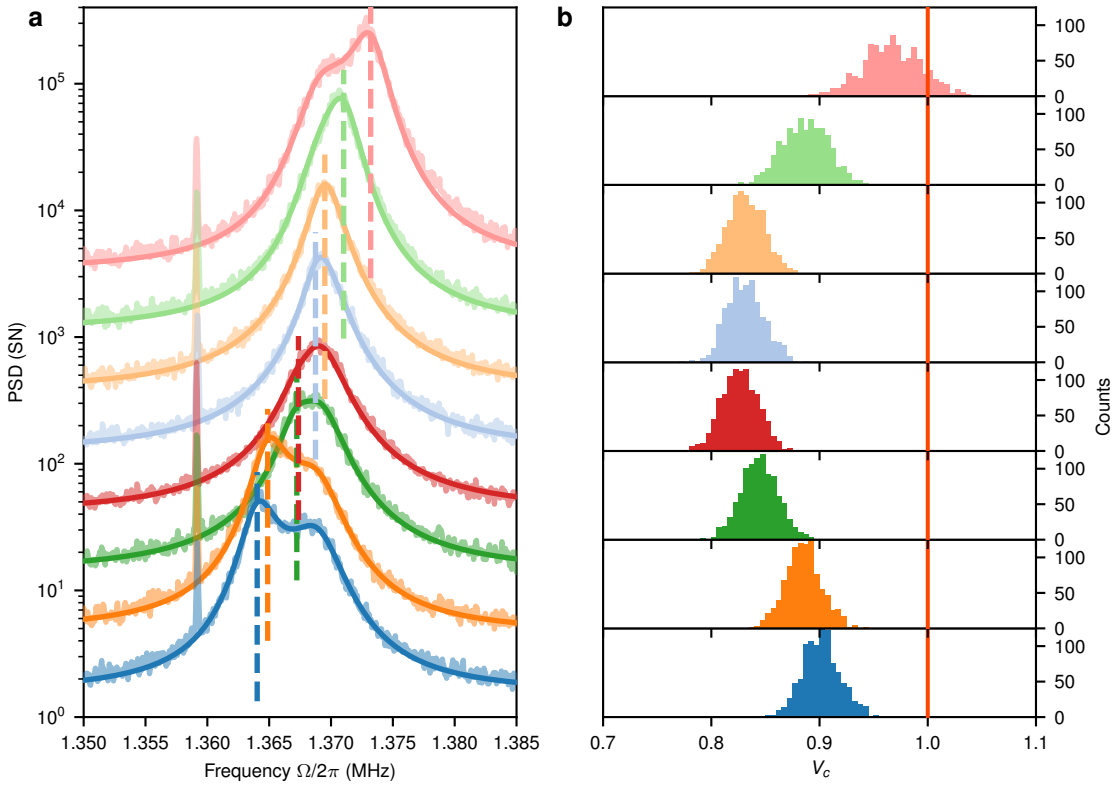

Figure SI8. **Entanglement tuning and optimisation. a,** Fit results for varied atomic frequencies ω_S for all points shown in Fig. 4. For clarity, subsequent lines are offset vertically by multiplying by a constant factor. **b,** MCMC results for the conditional variance for all atomic detunings. Mean and standard deviation leads to the points in Fig. 4b.

periodogram estimator, and additional uncertainty due to shot-noise level calibration. We additionally assume the level of data uncertainty to have an extra constant offset of 0.1 SN units to account for the presence of small mirror mode peaks beneath the signal.

Due to the vast parameter space, originating partly from the collective fitting with both shared and non-shared parameters, we perform the optimisation with Markov Chain Monte Carlo (MCMC) simulations [19]. We run 150 walkers with 4000 burn-in steps and subsequent 6000 sampling steps. From these 900 000 points, we select 1000 random samples for which we compute entanglement. This sampling of the log-likelihood landscape leads directly to posterior probabilities for the parameters for each spectrum, and, more importantly, also for derived values, such as the conditional variance. The choice of the number of samples for the entanglement calculation is determined by the computational cost of evaluating the conditional variance. Sampling those 1000 points from a larger set of MCMC points reduces the co-variance of the points sampling of the posterior log-likelihood landscape.

The MCMC fitting routine results in a set of parameters with good agreement between priors and posteriors for almost all parameters. The main discrepancy is for the case of inter-system quantum efficiency; here, the posterior value of $\nu = 0.53$ is significantly lower than the anticipated value of $\nu_{\mathrm{prior}} = 0.65 \pm 0.03$. In addition, we obtain a slightly lower posterior detection efficiency $\eta = 0.77$ than $\eta_{\mathrm{prior}} = 0.80 \pm 0.03$ and higher overcoupling $(\kappa_{\mathrm{in}}/\kappa) = 0.925 \pm 0.005$ than $(\kappa_{\mathrm{in}}/\kappa)_{\mathrm{prior}} = 0.91 \pm 0.01$. The extra optical losses are currently unaccounted for, with possible explanations for this discrepancy that include mode matching and polarisation-dependent losses of our quantum signal. We should stress that this discrepancy leads only to a reduction of the obtained entanglement. The atomic parameters are kept reasonably within the prior bounds with $\Gamma_{\mathrm{S,prior}}/2\pi = (18 \pm 1)\,\mathrm{kHz}$ and posterior $\Gamma_{\mathrm{S}}/2\pi = (20.3 \pm 0.4)\,\mathrm{kHz}$ as well as $n_{\mathrm{S,prior}} = 0.72 \pm 0.05$ and posterior $n_{\mathrm{S}} = 0.81 \pm 0.05$.

[*] These authors contributed equally to the work
[*,†] These authors contributed equally to the work; Currently at: ICFO – Institut De Ciencies Fotoniques, The Barcelona Institute of Science and Technology, Castelldefels, Spain
[‡] Currently at: Pritzker School of Molecular Engineering, University of Chicago, Chicago, USA
[§] Currently at: Danish Fundamental Metrology, Hørsholm, Denmark
[¶] Corresponding author: polzik@nbi.ku.dk

[1] Balabas, M. V. *et al.* High quality anti-relaxation coating material for alkali atom vapor cells. *Opt. Express* **18**, 5825–5830 (2010).
[2] Julsgaard, B., Sherson, J., Sørensen, J. L. & Polzik, E. S. Characterizing the spin state of an atomic ensemble using the magneto-optical resonance method. *Journal of Optics B: Quantum and Semiclassical Optics* **6**, 5 (2004).
[3] Agarwal, G. S. & Chaturvedi, S. Scheme to measure quantum stokes parameters and their fluctuations and correlations. *Journal of Modern Optics* **50**, 711–716 (2003).
[4] Borregaard, J. *et al.* Scalable photonic network architecture based on motional averaging in room temperature gas. *Nature Communications* **7**, 11356 (2016).
[5] Thomas, R. A., *et al.* Atomic Spin System Calibrations by Coherently Induced Faraday Rotation. In preparation.
[6] Weis, S. *et al.* Optomechanically induced transparency. *Science* **330**, 1520–1523 (2010).
[7] Møller, C. B. *et al.* Quantum back-action-evading measurement of motion in a negative mass reference frame. *Nature* **547**, 191–195 (2017).
[8] Tsaturyan, Y., Barg, A., Polzik, E. S. & Schliesser, A. Ultracoherent nanomechanical resonators via soft clamping and dissipation dilution. *Nature Nanotechnology* **12**, 776–783 (2017).
[9] Jayich, A. M. *et al.* Dispersive optomechanics: A membrane inside a cavity. *New Journal of Physics* **10**, 095008 (2008).
[10] Nielsen, W. H. P., Tsaturyan, Y., Møller, C. B., Polzik, E. S. & Schliesser, A. Multimode optomechanical system in the quantum regime. *Proceedings of the National Academy of Sciences* **114**, 62–66 (2017).
[11] Julsgaard, B. *Entanglement and Quantum Interactions with Macroscopic Gas Samples.* PhD dissertation, University of Aarhus (2003).
[12] Wasilewski, W. *et al.* Generation of two-mode squeezed and entangled light in a single temporal and spatial mode. *Opt. Express* **17**, 14444–14457 (2009).
[13] Carmichael, H. *An Open Systems Approach to Quantum Optics* (Springer, Berlin, Heidelberg, 1993).
[14] Helstrom, C. W. *Quantum detection and estimation theory* (Academic Press, 1976).
[15] Müller-Ebhardt, H. *et al.* Quantum-state preparation and macroscopic entanglement in gravitational-wave detectors. *Phys. Rev. A* **80**, 043802 (2009).
[16] Miao, H. *Exploring Macroscopic Quantum Mechanics in Optomechanical Devices.* Ph.D. thesis, University of Western Australia (2010).
[17] Broersen, P. M. T. *Automatic Autocorrelation and Spectral Analysis* (Springer-Verlag, Berlin, Heidelberg, 2006).
[18] Wiener, N. *Extrapolation, Interpolation, and Smoothing of Stationary Time Series: With Engineering Applications.* Massachusetts Institute of Technology : Paperback series (M.I.T. Press, 1964).
[19] Foreman-Mackey, D., Hogg, D. W., Lang, D. & Goodman, J. emcee: The MCMC hammer. *Publications of the Astronomical Society of the Pacific* **125**, 306–312 (2013).

Parameter	Symbol	Value
	Atomic spin oscillator	
Decoherence rate in the dark	$\gamma_{\mathrm{S0,dark}}/2\pi$	450 Hz
Intrinsic linewidth	$\gamma_{\mathrm{S0}}/2\pi$	1.7 kHz
Effective linewidth (incl. dynamical damping)	$\gamma_{\mathrm{S}}/2\pi$	2.9 kHz
Tensor contribution	ζ_{S}	0.028
LO_1 driving power		350 µW
Readout rate	$\Gamma_{\mathrm{S}}/2\pi$	20 kHz
Spin Polarisation	p	0.82
Spin thermal occupancy	n_{S}	0.8
Microcell temperature		50°C
	Mechanical oscillator and cavity	
Intrinsic mechanical frequency	$\omega_{\mathrm{M0}}/2\pi$	1.370 MHz
Intrinsic damping rate	$\gamma_{\mathrm{M0}}/2\pi$	2.1 mHz
Optical damping rate	$\gamma_{\mathrm{M}}/2\pi$	3.9 kHz
Cavity detuning	$\Delta/2\pi$	−0.7 MHz
Total cavity linewidth	$\kappa/2\pi$	4.2 MHz
LO_2 drive power		∼8 µW
Intracavity photons	N	1.6×10^6
Single photon coupling rate	$g_0/2\pi$	6×10^1 Hz
Readout rate	$\Gamma_{\mathrm{M}}/2\pi$	15 kHz
Cavity overcoupling	$\kappa_{\mathrm{in}}/\kappa$	0.93
Thermal bath temperature	T	11 K
Bath occupancy	n_{M0}	173×10^3
Mean occupancy	n_{M}	~ 2
Quantum cooperativity	$C_{\mathrm{q}}^{\mathrm{M}}$	15
	Hybrid & detection	
Quantum efficiency between systems	ν	0.53
Cavity mode-matching (amplitude)		0.9
Power transmission between systems		0.8
Detection efficiency	η	0.77
Homodyning visibility		0.96
Power transmission and detector QE		0.87
LO_1–LO_2 phase	φ	∼180°
Detection phase	ϑ	2°

Table SI1. **Summary of notation and experimental parameters.** When applicable, we quote the posterior mean values from the MCMC simulation.